

Article

Not peer-reviewed version

---

# Movable Automata for Simulation of Boundary Conditions and Shear Flow of Fluids Systems

---

[Alexander E. Filippov](#) , [Mikhail Popov](#) <sup>\*</sup> , [Valentin L. Popov](#) <sup>\*</sup>

Posted Date: 10 June 2025

doi: 10.20944/preprints202506.0785.v1

Keywords: friction; movable digital automata; atomically flat surface; effective temperature; ordered structure



Preprints.org is a free multidisciplinary platform providing preprint service that is dedicated to making early versions of research outputs permanently available and citable. Preprints posted at Preprints.org appear in Web of Science, Crossref, Google Scholar, Scilit, Europe PMC.

Copyright: This open access article is published under a Creative Commons CC BY 4.0 license, which permit the free download, distribution, and reuse, provided that the author and preprint are cited in any reuse.

## Article

# Movable Automata for Simulation of Boundary Conditions and Shear Flow of Fluids Systems

A.E. Filippov <sup>1</sup>, M. Popov <sup>2,\*</sup> and V.L. Popov <sup>1,3,\*</sup>

<sup>1</sup> Department of System Dynamics and Friction Physics, Technische Universität Berlin, Berlin, 10623, Germany, filippov\_ae@yahoo.com

<sup>2</sup> Department of Artificial Intelligence and Information Systems, Samarkand State University, Samarkand, Uzbekistan

<sup>3</sup> Center of Advanced Studies in Mechanics, Tribology, Bio- and Nanotechnologies, Samarkand State University, Samarkand 140104, Uzbekistan, v.popov@tu-berlin.de

\* Correspondence: mpopov@fastmail.fm, v.popov@tu-berlin.de

**Abstract:** The present work aims to develop a simple simulation tool capable of modeling the boundary conditions between a solid and a fluid. We study friction between two atomically flat surfaces composed of particles of different sizes and separated by a model fluid formed by moving particles with repulsing cores of different sizes and a long-range attraction. The suggested simulation method is shown to demonstrate realistic behavior at different parameters of interaction and loading, such as temperature, external pressure and mutual relative velocity of the surface plates. A systematic study of the model is performed for a system with uniformly sized particles. It is shown that fluid particles can form different (solid, liquid and gaseous) states, depending on the effective temperature (kinetic energy, caused by surface motion and random noise generated by spatially distributed Langevin sources). The behavior of the system is determined by two main factors: the relative radius of the “fluid” and “surface” particles and by the parameters of adhesive interaction. Heating the region close to one of the plates can change the density of the liquid in its proximity and result in chaotization (turbulence), and also dramatically change the configuration, the direction of the average flow, and reduce effective friction force.

**Keywords:** friction; movable digital automata; atomically flat surface; effective temperature; ordered structure

## 1. Introduction

The classical no-slip boundary condition—assuming that a fluid in contact with a solid surface adopts the same velocity as that surface—has long served as a cornerstone of macroscopic hydrodynamics. However, mounting evidence from nanotribology and nanofluidics challenges the generality of this assumption, revealing conditions under which fluids can exhibit slip at solid boundaries. Notably, these deviations arise not only due to confinement effects and surface structure, but also as a result of molecular-level interactions that alter the effective boundary conditions [1,2].

One striking manifestation of such phenomena is the emergence of slip behavior reminiscent of dry friction effects, where interfacial shear stresses can surpass a critical threshold and initiate sliding between the fluid and the solid [1,3]. This suggests that fluids under certain conditions can behave analogously to amorphous solids, allowing the definition of a “static friction threshold” at the liquid-solid interface. Particularly on atomically smooth surfaces such as mica or graphene, the principles underlying *structural superlubricity* in solids may likewise govern fluid slip behavior [4,5].

Another intriguing aspect is the concept of *liquid superlubricity*, wherein van der Waals repulsion—previously demonstrated between solid bodies—may reduce or even eliminate friction at the liquid-solid interface [6]. Theoretical frameworks, dating back to Lifshitz and collaborators, provide conditions under which repulsive van der Waals forces emerge [7]. When such repulsion

occurs, it effectively maintains a nanoscopic separation between surfaces, weakening molecular adhesion and facilitating near-frictionless sliding [8,9].

Further complexity arises in non-ideal interfaces, where partial adhesion and tangential slip can generate negative interfacial pressures, potentially inducing cavitation or interfacial fracture [10,11]. These instabilities may propagate in ways analogous to crack dynamics in solids, thereby stabilizing slip once it is initiated. Such behavior suggests deeper analogies between tribological phenomena in liquids and those traditionally associated with solid mechanics [12].

Despite increasing recognition of these effects, systematic studies of the conditions that govern slip onset, frictional resistance, and the interplay with surface properties remain scarce. This paper aims to fill this gap through a comprehensive investigation combining molecular dynamics simulations, non-equilibrium thermodynamics, and mesoscale modeling. In doing so, we seek to uncover the key parameters controlling interfacial slip in fluid-solid contacts and to establish theoretical foundations for tailoring hydrodynamic boundary conditions in both nano- and macroscale systems. As part of this aim, in the present paper we describe a simple numerical model capable of simulating various phase states and solid-fluid interactions. Its application to investigation of boundary conditions between solids and fluids will be carried out in a follow-up paper.

## 2. Choice of Numerical Method

Modeling complex fluid motion—particularly turbulent flow—is typically computationally intensive when using traditional continuum mechanics, which assumes a smooth velocity field. In this study, we adopt a computational approach based on a discrete representation of the continuum. Our objective is to construct a robust yet simple model capable of capturing the key phenomena relevant to our investigation. Specifically, we focus on how mesoscopic and macroscopic properties—and the associated geometrical patterns—emerge from underlying dynamic processes.

A suitable framework for this analysis is provided by discretizing the continuum and simulating the dynamics of discrete automata (meso-particles) that represent it. For instance, the model proposed in [13], which is based on discrete particle dynamics with repulsive interactions, can reproduce a wide spectrum of mass and energy transport regimes—from solid-like to gas-like behavior. This approach allows control over the correlation radius between particles, a parameter that effectively tunes the material's response in terms of flow and stress.

Traditional molecular dynamics, which models atomic or molecular motion directly, remains limited in accessible spatial and temporal scales, which limits its feasibility for studies such as this. Instead, we use “particles” representing a system of mesoscopic entities whose collective motion captures the essential system behavior. Notably, this modeling strategy has recently enabled significant advances in understanding structural lubricity in both soft and hard matter systems [13].

Various discretization methods—such as the method of movable cellular automata [14], smoothed particle hydrodynamics, and the discrete automata method [15] - have shown both qualitative and, in many cases, quantitative agreement with experimental results. Our work also follows this approach, with an emphasis on computational efficiency and on extracting qualitative insights from numerical simulations, along with facilitation of intuitive visualization across a broad range of scenarios and time frames. To this end, we adopted the isotropic movable automata technique, which features a combination of short-range repulsive and weak long-range attractive forces between particles.

The form of the interparticle potential ensures the presence of a well-defined minimum and an associated equilibrium configuration. As a result, the system spontaneously forms compact structures without the need for explicit boundary constraints. Even when the average particle density is below the threshold for continuous space-filling, there is a natural tendency for particles to aggregate. It has been shown [13] that when the kinetic energy density  $E_{kin} \gg C_{ij}$ , where  $C_{ij}$  is a stiffness parameter associated with the magnitude of the attractive interaction between particles  $i$  and  $j$ , the system behaves like a gas of nearly free-flying particles. In the opposite limit case,  $E_{kin} \ll C_{ij}$ , a crystal lattice is formed spontaneously.

In the gaseous state, the system exhibits isotropy on average. In the solid state, the lattice assumes hexagonal symmetry, assuming an isotropic interaction potential. In both limits, the system demonstrates regular dynamic behavior. However, the transition between these states—due to differing symmetries—passes through a disordered intermediate state. In the presence of dissipation, this state behaves as a viscous fluid.

Thus, this minimalist model is capable of efficiently capturing the full range of aggregate states—solid, liquid, and gas. It offers a versatile and practical framework for studying systems undergoing transitions between different physical states under varying conditions, including internal and external friction.

### 3. General Basic Model

The model structure in the present paper generally follows analogous models already used in large number of previous works [17–26]. The model is therefore only introduced briefly, with a focus on the main changes which are applied in this paper. In the movable automata approach, one deals with a system of  $N$  movable objects (effective particles). As usual, they are represented by the vector radius  $\mathbf{r}_i$ , the momentum  $\mathbf{p}_i$ , and the interaction potential  $U(|\mathbf{r}_i - \mathbf{r}_j|)$  corresponding to the following Hamiltonian (see for example course of theoretical physics Landau and Lifshitz, 1976 [25]):

$$H(\mathbf{r}_i, \mathbf{p}_i) = \sum_{i=1}^N \mathbf{p}_i^2 / 2m + \sum_{i,j=1}^N U(|\mathbf{r}_i - \mathbf{r}_j|) / 2 \quad (1)$$

The main idea used in our previous papers was to simulate a liquid (gas) using a simple interaction potential defined by a pair of Gauss potentials:

$$U(|\mathbf{r}_i - \mathbf{r}_j|) = C_{ij} \exp\{-(|\mathbf{r}_i - \mathbf{r}_j| / c_{ij})^2\} - D_{ij} \exp\{-(|\mathbf{r}_i - \mathbf{r}_j| / d_{ij})^2\}, \quad (2)$$

where  $C_{ij}$  and  $D_{ij}$  define the magnitude, while  $c_{ij}$  and  $d_{ij}$  are the radii of attraction and repulsion, and relation between the parameters is:  $C_{ij} \gg D_{ij}$ ,  $c_{ij} < d_{ij}$ . The equations of motion have the following form:

$$m \partial \mathbf{v}_i / \partial t = -\partial H(\mathbf{r}_i, \mathbf{p}_i) / \partial \mathbf{r}_i + \mathbf{f}_i \quad (3)$$

$\mathbf{v}_i$  is the velocity of the  $i$ -th particle, the forces  $\mathbf{f}_i$  will be explained further. All the unknown or stochastic influences should be incorporated according to fluctuation-dissipation theorem with effective temperature  $T_{eff}$ . As usual, it is simulated by random  $\delta$ -correlated Langevin [23], having the correlators:

$$\langle \xi(t, \mathbf{r}_i) \xi(t', \mathbf{r}_j) \rangle = D \delta(t - t') \delta_{ij}, \quad (4)$$

where  $\langle \xi(t, \mathbf{r}_i) \rangle = 0$  and the diffusion coefficient is proportional to temperature  $D \sim T$ . By varying intensity of noise at fixed interactions or vice versa, the system can represent different states from gaseous to liquid and solid ones [13]–[17]. Below, we will always suppose that this relation is chosen to simulate *liquid*.

There are different options to numerically simulate liquid motion between two solid interfaces. For example, in the simplest case, the liquid can be confined between two planar rigid repulsing planes:  $z = z_{down}$  (lower plane) and  $z = z_{up} \equiv L_z$  (upper plane). Numerically, this can be done by means of reflecting boundary conditions with sharp repulsing potentials exponentially growing inside the boundary walls:  $U_{up} = C \exp[(z - L_z) / c]$  and  $U_{down} = C \exp[(z_{down} - z) / c]$ .

Since the system is composed of discrete, movable particles, the following computational procedure was adopted for our previous numerical experiments: Initially, a fixed number of particles were randomly distributed within a rectangular domain with sides  $L_x$  and  $L_z$ . To allow the system to relax, it was first brought to near-zero temperature, enabling the particles to interact and self-



organize into a near-equilibrium configuration characterized by multiple domains with varying orientations. Following this initialization phase, shear flow was induced by moving the top and bottom boundaries in opposite horizontal directions. In a perfectly laminar regime, the resulting velocity profile along the vertical (ordinate) axis would be smooth and monotonic, reflecting a uniform shear across the system.

However, this behavior changes significantly when the material is partitioned into distinct domains. Initially, the structure responds elastically, with lattice nodes smoothly following the displacement of the shearing boundaries. This results in a continuous velocity gradient across the system. When the applied shear strain surpasses a critical threshold, bonds between certain neighboring particles begin to break, allowing the formation of new local configurations.

While all particles are theoretically coupled through long-range interactions, their actual dynamics are dominated by their immediate neighbors. As a result, localized regions of the lattice tend to move collectively, maintaining their internal order while shifting crystallographic planes primarily at domain boundaries.

Here, as in our previous studies, we apply Delaunay triangulation to identify the nearest neighbors and evaluate the local connection symmetry. This is particularly important for identifying defect chains (characterized by 5-fold and 7-fold symmetry) and domain boundaries.

#### 4. Model Modification and Evaluation

The original model described in our previous works [13,17,25,26] and others, used a maximally simple interaction potential defined by a pair of Gaussians:  $U(|\mathbf{r}_i - \mathbf{r}_j|) = C_{ij} \exp\{-(|\mathbf{r}_i - \mathbf{r}_j|/c_{ij})^2\} - D_{ij} \exp\{-(|\mathbf{r}_i - \mathbf{r}_j|/d_{ij})^2\}$  where parameters  $C_{ij}$ ,  $D_{ij}$ ,  $c_{ij}$  and  $d_{ij}$  permitted to regulate the magnitude and the radii of attraction and repulsion. Generally, the magnitude relation between these parameters:  $C_{ij} \gg D_{ij}$ ,  $c_{ij} < d_{ij}$  simulates the interaction of particles well enough if their repulsive core is not very important. Mathematically such potentials allowed the particles partially penetrate one into another. In the majority of cases such partial interpenetration did not affect the physical picture when the collective behavior (at mesoscopic scales) is considered. The same is true in relation to the interaction between the particles and substrates.

In many friction and shear problems the contact surface is either treated as “atomically flat”, or mesoscopically fractal, where fine structure of the interaction between the particles is not so important. However, below we will be interested in the effects of commensurability or incommensurability. With this goal in mind, we modify the model to make the interaction qualitatively closer to the Lennard-Jones potential defining a very hard central core with almost vertical potential walls and a narrow attraction belt around the core but still conserving mesoscopic size of the “particles” to use them as classical, relatively large “movable automata”.

It is important for further consideration to maintain the flexibility to study the interaction between particles, since we will consider not only interaction inside the fluid, but also interaction with the automata/particles of the upper and bottom surfaces as well. These automata are supposed to simulate objects that are qualitatively different from the internal ones. Assuming that in the equations of motion only the forces between objects are used, it is convenient to construct here, instead of the potential Eq.2, the following interaction force:

$$f(|\mathbf{r}_i - \mathbf{r}_j|) = f_{repuls}(\mathbf{r}_i - \mathbf{r}_j) - f_{attract}(\mathbf{r}_i - \mathbf{r}_j) \quad (5)$$

with

$$f_{repuls}(|\mathbf{r}_i - \mathbf{r}_j|) = C_{ij} 1/[1 + E_{repuls}(|\mathbf{r}_i - \mathbf{r}_j|; R_i^{repuls}; R_j^{repuls})];$$

$$f_{attract}(|\mathbf{r}_i - \mathbf{r}_j|) = D_{ij} 1/[1 + E_{attract}(|\mathbf{r}_i - \mathbf{r}_j|; R_i^{attract}; R_j^{attract})].$$

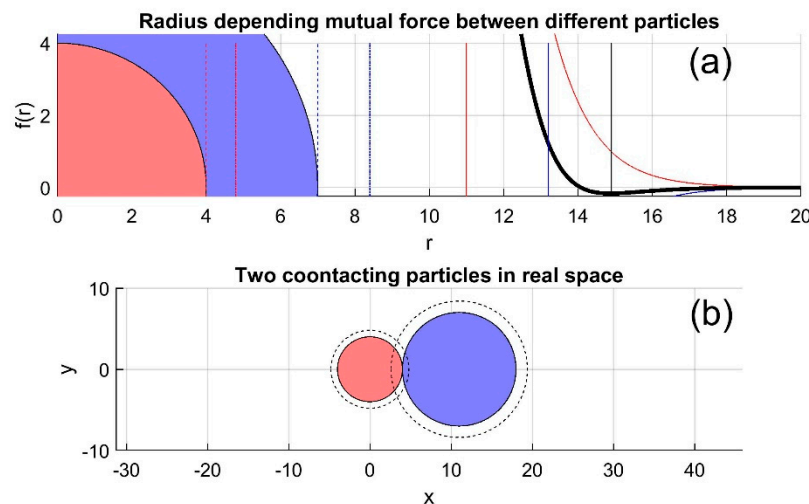
and

$$E_{repuls}(|\mathbf{r}_i - \mathbf{r}_j|; R_i^{repuls}; R_j^{repuls}) = \exp[(-(|\mathbf{r}_i - \mathbf{r}_j| - (R_i^{repuls} + R_j^{repuls}))) / c] \quad (6)$$

$$E_{attract}(|\mathbf{r}_i - \mathbf{r}_j|; R_i^{attract}; R_j^{attract}) = \exp[(-(|\mathbf{r}_i - \mathbf{r}_j| - (R_i^{attract} + R_j^{attract}))) / d], \quad (7)$$

Every combination of  $1/(1+\exp(\dots))$  works here as a smooth step-like (Fermi-Dirac) function with the radius equal to the sum  $R = R_i + R_j$ , and the amplitude and width of the step being regulated by combination of the parameters  $C_{ij}$ ,  $D_{ij}$ ,  $c_{ij}$  and  $d_{ij}$ . At large distances such functions work similarly to the forces caused by the Gaussians in Eq.2. However, if these amplitudes are large enough and the widths of the smoothed step-functions are narrow, these interactions ensure sharp exponential walls around the repulsing core of each particle, with well-defined, but still easily varied distance between the centers  $R = R_i + R_j$  in each interacting pair.

Fig.1 illustrates the force-distance relationship between two particles of different radii. The total interaction force, shown in subplot (a), consists of two components: a strong short-range repulsion and a weaker but longer-range attraction. This attractive component forms an "adhesive belt" surrounding the nearly rigid core of each particle. Subplot (b) schematically depicts two such particles in contact, with their adhesive belts overlapping, indicated by dashed circles.



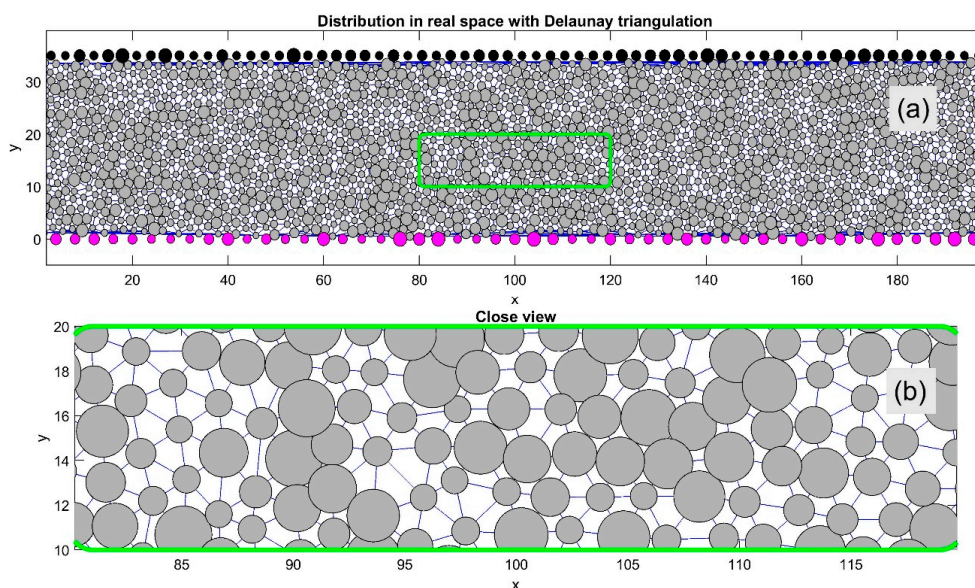
**Figure 1.** Schematic of the distance-dependent interaction force between two particles of different radii. (a) strong short-range repulsive core and a much weaker long-range attractive potential. (b) Two particles in contact.

Figure 2 demonstrates the practical applicability of the interaction forces defined in Eqs. (5–7). It shows a typical instantaneous particle distribution between the upper and lower surfaces. These surfaces are covered with stationary particles (depicted in black and magenta), which move in opposite horizontal directions. The same interaction rules apply to these surface-bound particles as to the internal ones.

The internal particles in Figure 2 are interconnected using Delaunay triangulation (thin lines), which allows for rapid identification of each particle's nearest neighbors. This triangulation is essential for characterizing the system's structural order and its temporal evolution. For better visualization, a magnified view of the central region (highlighted by a green rectangle in subplot (a)) is shown in subplot (b). The main system includes a diverse mix of particles with varying radii  $R = R_i + R_j$ , and their dynamic behavior is further illustrated in **Supplementary Movie Test.mp4**. This video shows spontaneous ordering and motion of particles between two plates, including effects of mutual repulsion and aggregation, and how these behaviors relate to the boundaries.

Realistic boundary motion can be achieved based on the chosen simulation scenario and associated boundary conditions. For simplicity, particles may be confined within a rectangular domain with reflective vertical and horizontal boundaries. However, for more realistic modeling,

vertical boundary positions are allowed to move according to a balance of external and internal forces. To simulate quasi-infinite motion in the horizontal direction (which enhances statistical reliability), periodic boundary conditions (i.e., cylindrical geometry) are used. This approach is employed in all supplementary movies, including **Supplementary Movie Test.mp4**.



**Figure 2.** Instantaneous particle distribution between oppositely moving upper and lower surfaces with fixed surface particles (black and magenta). Internal particles are linked by Delaunay triangulation (thin lines), used to identify nearest neighbors and analyze lattice order. A magnified view of the green-marked region is shown in subplot (b).

Figure 3 presents time-dependent correlations among several key system parameters: (a) the vertical position of the upper plate, (b) the horizontal force (interpreted as friction), and (c) the fractions of particles with five, six, and seven neighbors (colored green, deep red, and orange, respectively). The vertical blue lines indicate the end of the initial transient phase, during which the system self-organizes from a random initial configuration into an equilibrium state. During this period, the system spontaneously forms a hexagonal lattice, significantly increasing the proportion of particles with six neighbors—despite variations in particle size.

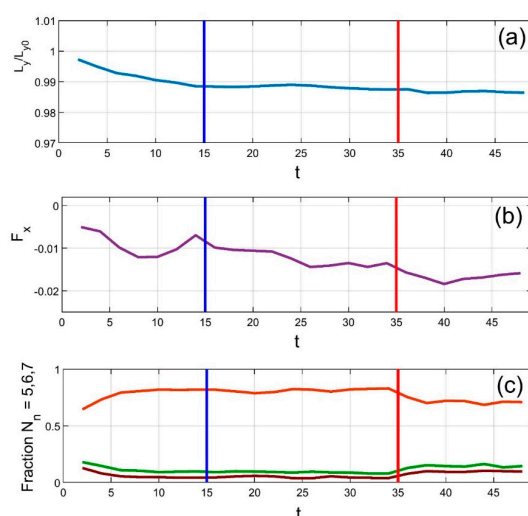


**Figure 3.** Time evolution of key system parameters: (a) upper plate position, (b) horizontal (friction) force, and (c) fractions of particles with 5, 6, and 7 neighbors (green, deep red, orange). The initial self-organization phase

ends at the blue line, after which a near-perfect hexagonal order emerges (6 neighbors dominate). Heating begins at the red line, disrupting the structure and increasing defects.

Remarkably, this ordered structure is maintained even during horizontal plate motion, up until the point when external heating is applied. This moment is marked by the vertical red line. As expected, the applied heating rapidly disrupts particle positions, increasing defects in the previously ordered hexagonal structure. In other words, the balance shifts from particles with six neighbors towards those with five or seven. This trend is clearly visible in subplot (c), where the orange curve (six neighbors) declines, while the other two rise.

Note that the colors of the curves—orange, green, and deep red—match those used in the scatter plot of Fig. 5 (see its description below). Also, due to the lack of a strict conservation law, the total count of particles with 5, 6, or 7 neighbors does not sum exactly to the total number of particles. This is because some particles have fewer or more neighbors. Near equilibrium, such anomalies are rare and have minimal impact on the system's collective behavior, so their time dependencies are omitted to avoid clutter.

The dynamic behavior from **Supplementary Movie Test.mp4** is captured in static form through time-space maps shown in Fig. 4, subplots (a) and (b). Here, the discrete particle distributions are smoothed into continuous density fields using Gaussian convolution and averaged along the horizontal axis. Instantaneous density and velocity distributions appear in subplots (c) and (d). These continuous values are also accumulated over time and displayed as color maps, with individual color bars in (a) and (b) reflecting different physical quantities.

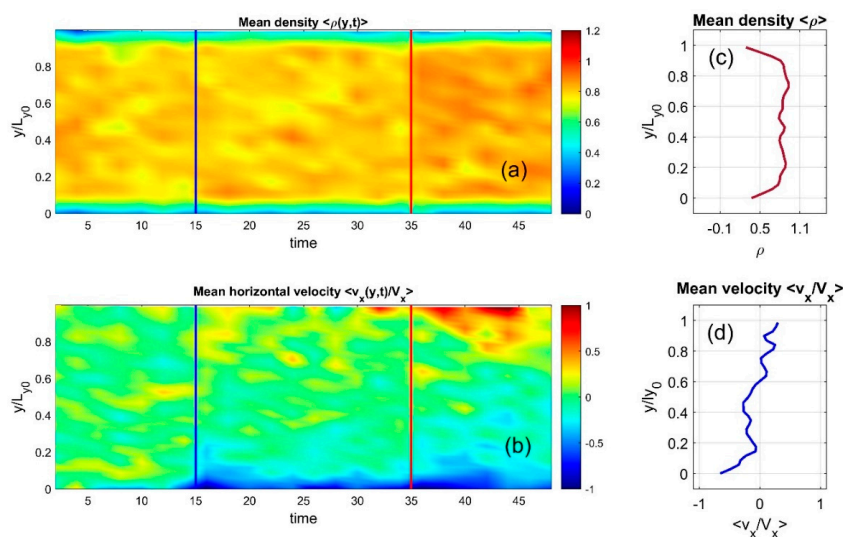


**Figure 4.** The dynamic evolution from Supplementary Movie *Test.01.mp4* is shown statically as time-space maps in subplots (a)–(b), where particle distributions are smoothed into continuous density using Gaussian convolution and averaged horizontally. Instantaneous density and velocity are shown in subplots (c) and (d), with accumulated values visualized using color maps.

After testing a general model with particles of varying sizes, we focus next on a simplified version with identical particles. Fig. 5 shows such a system, where all particles have equal radii, identical adhesion belts, and interaction parameters, simulated using the general model described in Figs. 1–2 at a fixed average density.

A spontaneously formed regular hexagonal structure is clearly visible in both subplots (a) and (b). This order is confirmed in subplot (b) by the dominance of orange-colored particles, indicating six neighbors. The system also exhibits distinct domains of hexagonal order, each with a different crystal lattice orientation.



In subplot (a), domain orientation is color-coded by the sine of the angle between each particle and its nearest neighbor. Domain boundaries are visible in subplot (b) as chains of defects—particles with five or seven neighbors—marked in green and deep red, respectively.

To complete the study, we also examine the system behavior at lower average densities. The results are presented in the following figures, Fig. 6 and Fig. 7.

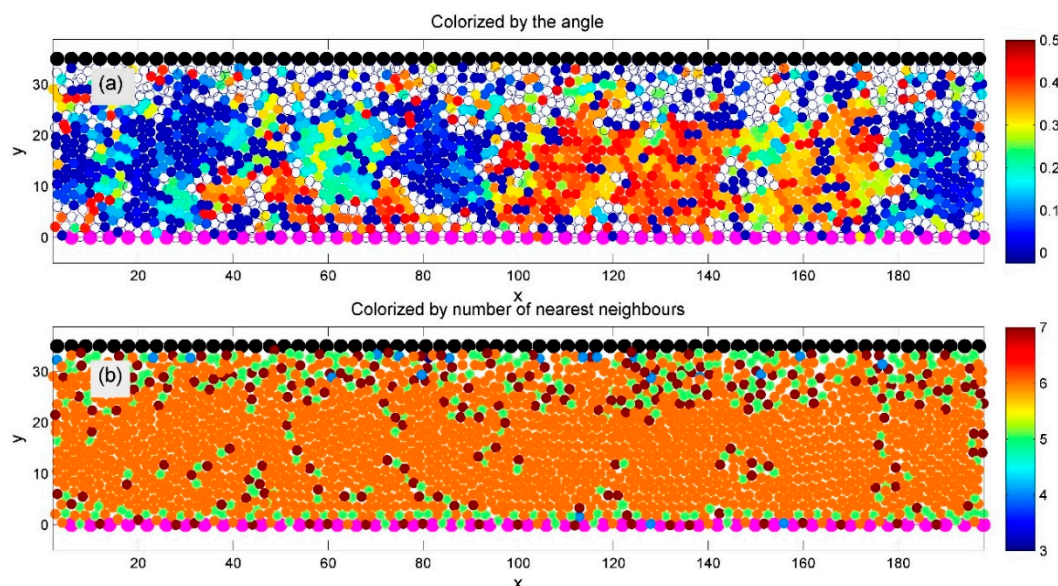


**Figure 5.** A regular model with identical particles (equal radii and interaction parameters) is simulated using the general setup from Figs. 1–2 at a given average density. After the initial transient phase, a well-ordered hexagonal structure emerges, indicated by orange-colored particles with six neighbors in subplot (b). Subplot (a) shows domains with different lattice orientations, colorized by the sine of the orientation angle. Domain boundaries, marked by chains of 5- and 7-fold defects, appear in green and deep red.

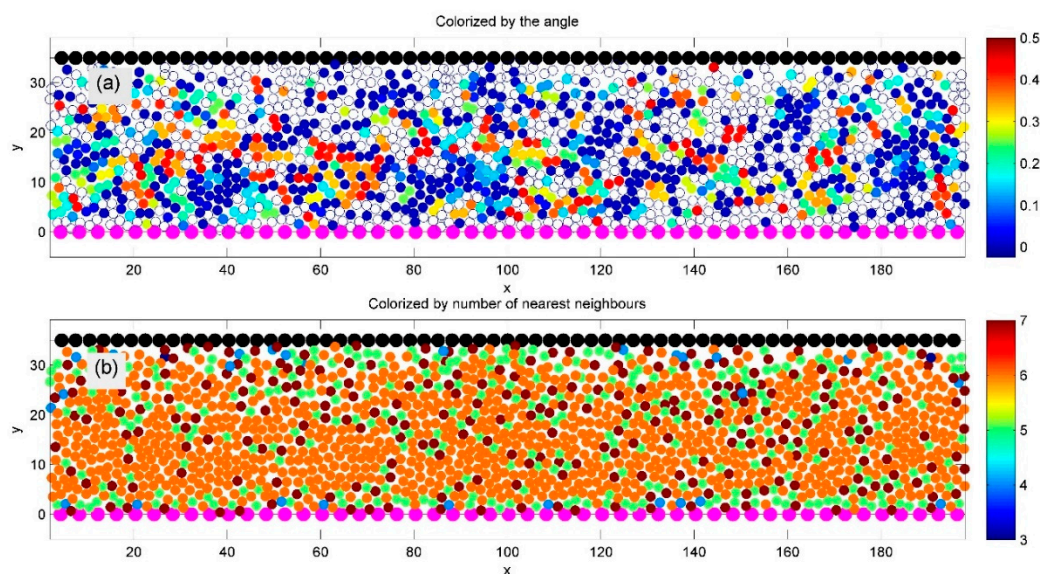


**Figure 6.** Similar to Fig. 5, but at lower average density. Subplot (b) still shows well-defined ordered domains (orange), though many particles now appear light blue, indicating fewer neighbors. Some less distinct domains with preferred crystal lattice orientations are also visible.

The systems shown in Figs. 6 and 7 are based on the same model as Fig. 5 but at lower average densities. In Fig. 6, ordered domains remain visible—particularly in subplot (b), where particles in these regions appear orange, indicating six neighbors. However, many particles are now light blue, reflecting a reduced number of neighbors in the Delaunay triangulation. Some domains with preferred lattice orientations are still distinguishable, though less clearly. In contrast, Fig. 7 shows no large orange domains; most particles are light blue, indicating a high level of structural defects and reduced symmetry.

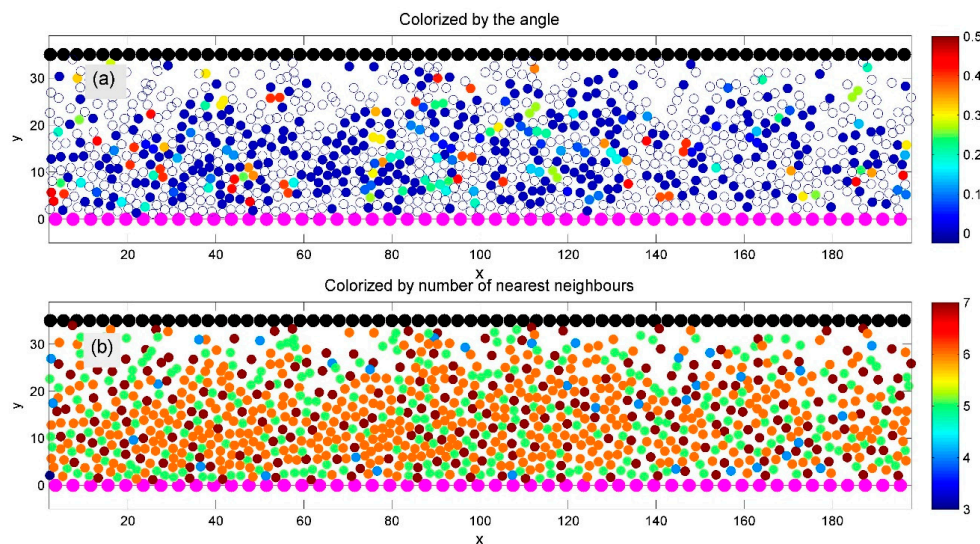


**Figure 7.** Same as Fig. 5 but at much lower density. Large orange domains are absent, and many more light blue particles indicate increased defects and lower symmetry.

Scatter plots provide a general visual overview of the system's structure and dynamics, but a continuous approach is more effective for quantitative analysis. To this end, we computed a continuous "order parameter" using Gaussian convolution to estimate local neighbor density, as shown in Fig. 8. In subplot (a), orange regions indicate areas with ideal hexagonal order.

Subplot (b) shows the time-dependent position of the upper boundary, determined by the balance between external vertical force and internal particle pressure (Eq. 8). Subplot (c) displays the total friction force resulting from the relative motion of the upper and lower boundaries.

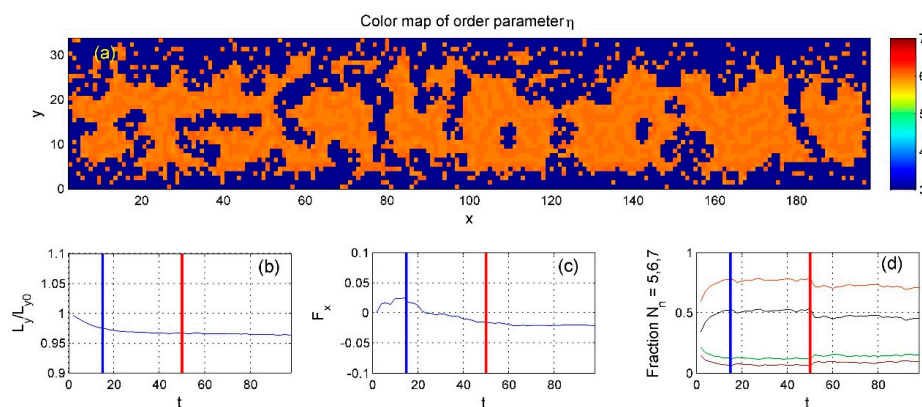


**Figure 8.** Continuous domain structure tracking system properties over time. Subplot (a) shows ideal hexagonal order (orange), (b) the upper boundary position, (c) total friction force—negative due to stronger lower-surface coupling—and (d) neighbor fractions with an order parameter (black) indicating structural order.



Subplot (d) shows the time-dependent fractions of particles with different coordination numbers, represented by green, orange, and red curves—matching the color scheme used in the scatter plots. The black curve shows the “order parameter,” defined as the difference between the fraction of six-neighbor particles and the sum of the other two. After heating begins (marked by the red line), this balance shifts, and the system becomes more disordered.

The same calculations were repeated for different average densities, with results shown in Figs. 9 and 10. The most notable difference in Fig. 10 is that the order parameter fluctuates around zero, indicating that the fraction of six-neighbor particles is roughly equal to the combined fraction of the others.

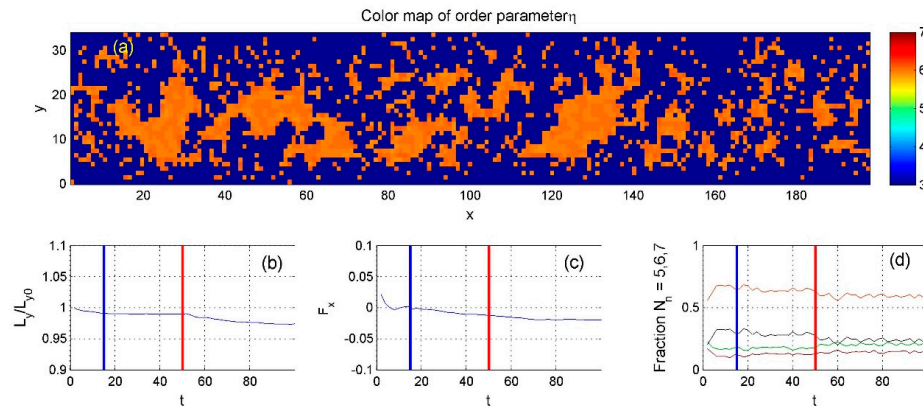


**Figure 9.** The same as in Fig.7 very lean with average density  $\rho \approx 3/4$ . The order parameter here is much smaller than in Fig.8.

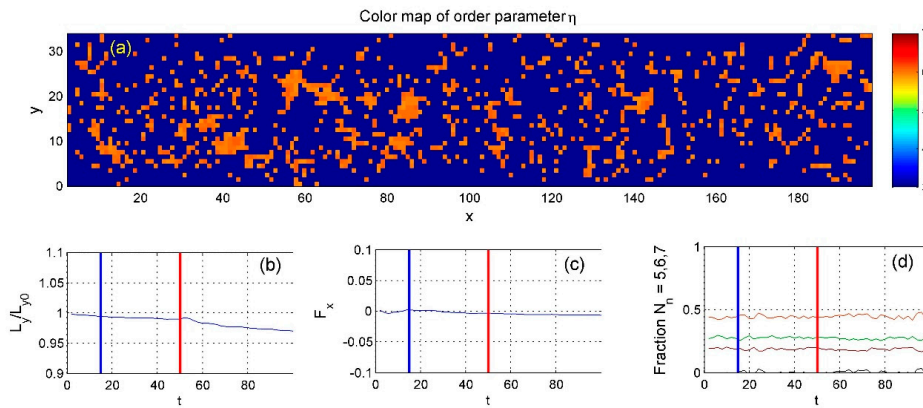


**Figure 10.** Same as Fig. 7 but with an even lower average density. Unlike Figs. 8 and 9, the order parameter here fluctuates around zero, indicating a balance between ordered and disordered particle states.

Now we are ready to establish simultaneous time evolution of the spatially distributed density  $\rho(x, z; t)$ , kinetic energy  $E_{kin}(x, y; t)$ , horizontal velocity  $v_x(x, z; t)$  and their values integrated along the x-coordinate:

$$\langle \rho(y; t) \rangle = \int_0^{L_x} dx \rho(x, y; t); \quad (8)$$

$$\langle E_{kin}(y; t) \rangle = \int_0^{L_x} dx E_{kin}(x, y; t); \quad (9)$$

$$\langle v_x(y; t) \rangle = \int_0^{L_x} dx v_x(x, y; t). \quad (10)$$

Although horizontal velocity is central to this study, both velocity components contribute to the formation of streamlines. Therefore, we calculated streamline maps at each time step, with and without heating. Their dynamic evolution—highlighting flow complexity and turbulence, especially under heating—is illustrated in **Supplementary Movie Stream.mp4**.

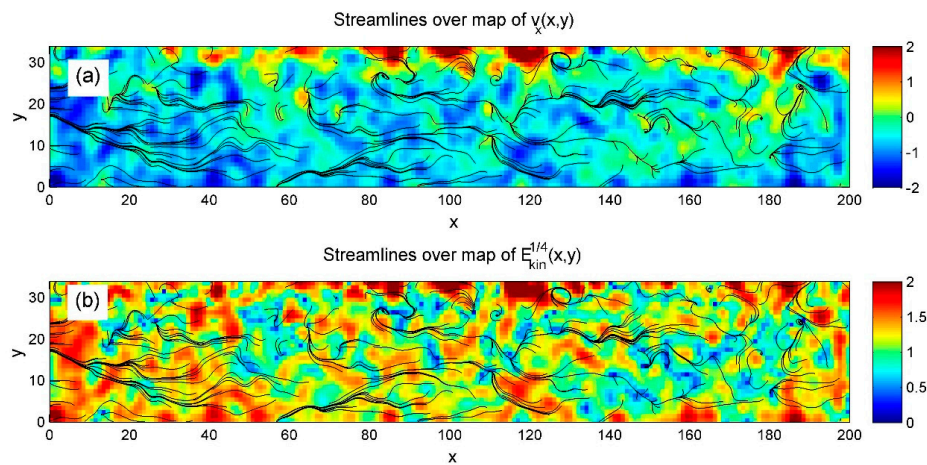


**Figure 11.** Streamlines from Gaussian-convolved data are shown over horizontal velocity (a) and kinetic energy (b) to highlight laminar flow in the bulk and turbulence near the heated upper surface. This contrast is especially clear in **Supplementary Movie Stream.mp4**.

The detailed flow complexity is not captured in the integrated time-dependent maps below. However, these integrations effectively reveal how key global values evolve over time as shear and heating are applied sequentially. As with the order parameter, we present the results as time-space diagrams. Summaries for three average densities are shown in Figs. 12–14 and the corresponding movies **Regular\_1.mp4**, **Regular\_2.mp4**, and **Regular\_3.mp4**.

These maps highlight the study's main findings. Initially, in the absence of heating, the dense system transitions into a near-laminar flow. The lower region, where surface particle spacing matches internal particle spacing, moves faster in the negative direction than the upper region, creating a vertical velocity gradient that becomes nearly linear (see **Regular\_1.mp4**).

When heating is applied, this velocity contrast increases. In the steady state, most of the system moves with the lower surface, while only the uppermost layers retain positive velocity. This shift appears as a step-like velocity profile in subplot (d) of Fig. 12. Although heating slightly affects the density distribution, this influence is minimal in the high-density case.

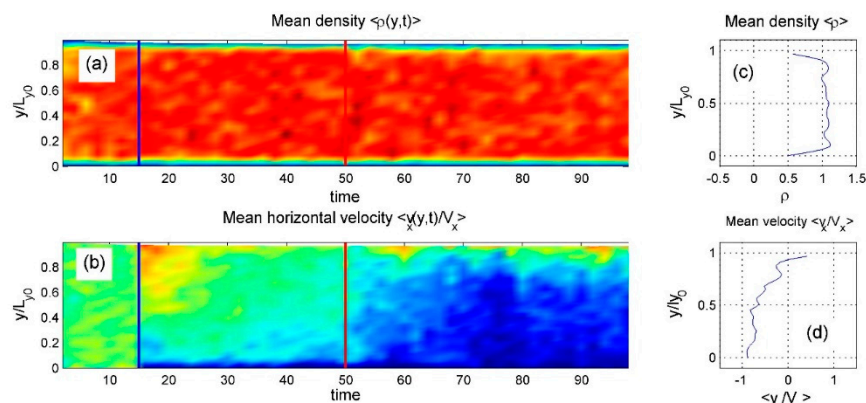


**Figure 12.** These space-time maps highlight a key result of the study: in a sufficiently dense system, heating from the upper surface causes the internal particles to follow the motion of the bottom surface, whose fixed particle spacing closely matches the typical distance between the mobile particles.



The intermediate-density system shows the richest behavior. As seen in **Regular\_2.mp4** and Fig. 13, the particle density redistributes during the process. Initially, without heating, internal particles move in the positive direction. Once heating is applied, the vertical density profile changes, altering the contact with the upper surface. After a transient phase, the internal particles reverse direction and begin moving negatively.

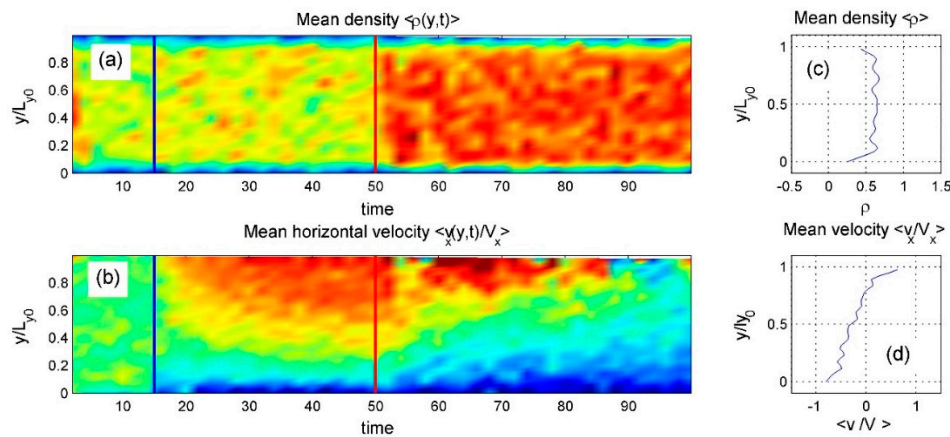


**Figure 13.** The same as in Fig.11 at smaller but still relatively large average density  $\rho \approx 3/4$  gradually redistributes in space to reduce interlocking with the commensurate lower substrate causing linear distribution of the velocity along vertical coordinate.

Finally, the time-dependent behavior of the low-density system is shown in **Regular\_3.mp4** and Fig. 14. Here, particle density concentrates near the center, reducing interlocking with both surfaces. Strong thermal fluctuations near the heated upper surface occasionally enhance or weaken coupling with the surface particles, shifting the velocity balance in favor of rightward motion. This behavior contrasts sharply with the leftward flow seen in Fig. 12.

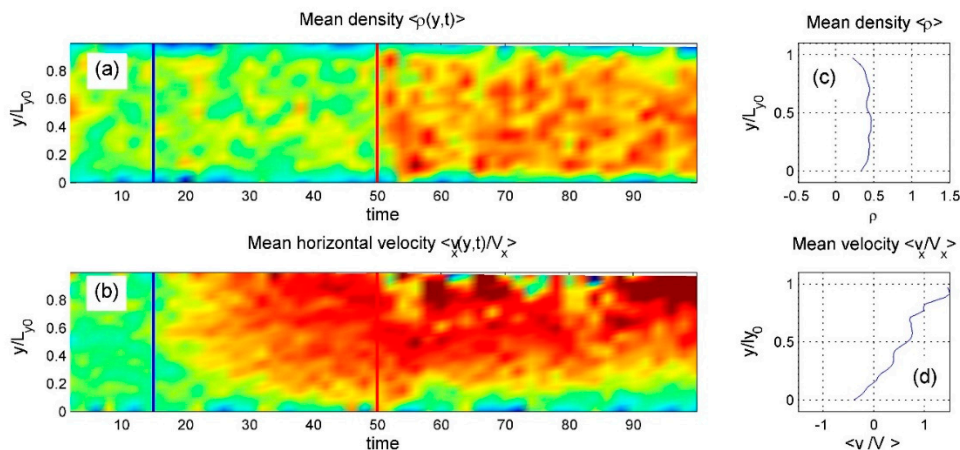


**Figure 14.** Same as Fig. 12, but at low density. Particles shift toward the center, reducing interlocking with both surfaces. However, thermal fluctuations near the heated upper surface occasionally enhance coupling, shifting overall motion to the right—opposite to the leftward flow in Fig. 12.

## 5. Conclusions

A particle-based numerical model for the study of friction between two atomically flat surfaces separated by a fluid was developed and characterized. It was shown that the model leads to realistic behavior at different parameters of interaction and loading modes, such as temperature, external pressure and mutual relative velocity of the surface plates. The system can assume solid, liquid and

gaseous states, depending on the effective temperature (kinetic energy, caused by surface motion and random noise generated by spatially distributed Langevin sources).

The main part of the study is devoted to testing the mode with a system composed of equal particles. It is established that the behavior of the system is mainly determined by the relative radius of the “fluid” and “surface” automata and by the parameters of adhesive interaction between them. It is shown also that alternative heating of the system in different regions close to one of the plates can change a density of the “liquid” in its proximity, provoke a chaotization of the liquid dynamics and result in dramatic transformation of the global structure and dynamics. Local heating can even essentially change direction of the average flow. Such an intensive restructuring of the process may have practical applicability for a significant reduction in friction in general.

**Supplementary Materials:** The following supporting information can be downloaded at the website of this paper posted on Preprints.org:

*Supplementary Movie Test.mp4*

This video demonstrates the dynamic evolution of particle configurations between two surfaces moving in opposite horizontal directions. The plates are coated with surface particles that are glued to them and color-coded in black and blue, respectively.

*Supplementary Movie Stream.mp4*

Dynamically changing (plotted with a discrete time-steps) continuous medium obtained by the Gaussian convolution of the movable discrete automata. The streamlines are plotted over the spatial densities of the horizontal velocity and kinetic energy to illustrate the contrast between the laminar flow inside the system and turbulence in the vicinity of heated upper substrate.

*Supplementary Movie Regular\_1.mp4*

Motion of the dense  $\rho \approx 1$  regular system (with equal radiuses for all particles) recorded dynamically. The scatter plot is colorized by number of nearest neighbors as shown by the colorbar. Integral values of the distance between the plates and friction force, as well as fractions of the subsystems with  $N_5$ ,  $N_6$  and  $N_7$  are plotted below the scatter. Time-space diagrams accumulating simultaneously with the dynamic process are depicted in the right panel of the movie. Integral density averaged over  $x$  and distribution of horizontal velocity depending on vertical coordinate  $y$  are plotted in the right subplots of this panel, respectively.

*Supplementary Movie Regular\_2.mp4*

The same as in the Supplementary movie Regular\_1.mp4 calculated at intermediate density  $\rho \approx 3/4$ . Of particular note are the changes in velocity distribution in the far-right subplot of the movie during the process, especially heating with heating enabled.

*Supplementary Movie Regular\_3.mp4*

The same as in the Supplementary movie Regular\_1.mp4 calculated at small density  $\rho \approx 1/2$ . One can notice dramatic chaotization of the motion produced by heating (in comparison to the original movie Regular\_1.mp4) accompanied by transformations of the velocity distribution shown in the far-right subplot.

**Author Contributions:** Conceptualization, V.L.P. and M.P.; methodology, V.L.P., M.P. and A.F.; software, A.F.; investigation, A.F.; writing—original draft preparation, A.F., M.P. and V.L.P.; writing—review and editing M.P., V.L.P.; supervision, V.L.P.; funding acquisition, V.L.P. All authors have read and agreed to the published version of the manuscript.

**Funding:** This research was funded by the Deutsche Forschungsgemeinschaft (DFG), project number 554322826 and by the Samarkand State University.

**Data Availability Statement:** The original contributions presented in this study are included in the article/supplementary material. Further inquiries can be directed to the corresponding authors.

**Conflicts of Interest:** The authors declare no conflicts of interest.

## References

1. Thompson, P.A.; Robbins, M.O. Shear flow near solids: Epitaxial order and flow boundary conditions. *Phys. Rev. A* 1990, 41, 6830–6837. <https://doi.org/10.1103/PhysRevA.41.6830>
2. Lauga, E.; Brenner, M.P.; Stone, H.A. Microfluidics: The no-slip boundary condition. In *Springer Handbook of Experimental Fluid Mechanics*; Springer: Berlin/Heidelberg, Germany, 2007; pp. 1219–1240. [https://doi.org/10.1007/978-3-540-30299-5\\_19](https://doi.org/10.1007/978-3-540-30299-5_19)
3. Popov, V.L. Contacts with negative work of “adhesion” and superlubricity. *Front. Mech. Eng.* 2020, 5, 73. <https://doi.org/10.3389/fmech.2019.00073>
4. Hod, O.; Meyer, E.; Zheng, Q.; Urbakh, M. Structural superlubricity and ultralow friction across the length scales. *Nature* 2018, 563, 485–492. <https://doi.org/10.1038/s41586-018-0704-z>
5. Socoliuc, A.; Bennewitz, R.; Gnecco, E.; Meyer, E. Transition from stick-slip to continuous sliding in atomic friction: Entering a new regime of ultralow friction. *Phys. Rev. Lett.* 2004, 92, 134301. <https://doi.org/10.1103/PhysRevLett.92.134301>
6. Han, T.; Zhang, S.; Zhang, C. Unlocking the secrets behind liquid superlubricity: A state-of-the-art review on phenomena and mechanisms. *Friction* 2022, 10, 1137–1165. <https://doi.org/10.1007/s40544-021-0586-1>
7. Dzyaloshinskii, I.E.; Lifshitz, E.M.; Pitaevskii, L.P. The general theory of van der Waals forces. *Adv. Phys.* 1961, 10, 165–209. <https://doi.org/10.1080/00018736100101281>
8. Meurk, A.; Luckham, P.F.; Bergström, L. Direct measurement of repulsive and attractive van der Waals forces between inorganic materials. *Langmuir* 1997, 13, 3896–3899. <https://doi.org/10.1021/la9610967>
9. Ye, Y.; Li, Y.; Lin, Q.; Zeng, S.; Zhou, X.; Zhang, C. Casimir repulsive-attractive transition between liquid-separated dielectric metamaterial and metal. *Phys. Rev. B* 2018, 98, 035410. <https://doi.org/10.1103/PhysRevB.98.035410>
10. Zhou, Y.; Wang, A.; Müser, M.H. How thermal fluctuations affect hard-wall repulsion and thereby Hertzian contact mechanics. *Front. Mech. Eng.* 2019, 5, 67. <https://doi.org/10.3389/fmech.2019.00067>
11. Pinon, A.V.; Klinke, C.; Berg, S.; Yamakov, V. Thermal effects on van der Waals adhesive forces. *Phys. Rev. B* 2016, 93, 035424. <https://doi.org/10.1103/PhysRevB.93.035424>
12. Levitas, V.I.; Idesman, A.V.; Palakala, A.K. Phase-field modeling of fracture in liquid. *J. Appl. Phys.* 2011, 110, 033531. <https://doi.org/10.1063/1.3619807>
13. Denisov, S.; Filippov, A.; Klafter, J.; Urbakh, M. From deterministic dynamics to kinetic phenomena. *Phys. Rev. E* 2004, 69, 042101. <https://doi.org/10.1103/PhysRevE.69.042101>
14. Vanossi, A.; Bechinger, C.; Urbakh, M. Structural lubricity in soft and hard matter systems. *Nat. Commun.* 2020, 11, 4657. <https://doi.org/10.1038/s41467-020-18429-1>
15. Monaghan, J.J. An introduction to SPH. *Comput. Phys. Commun.* 1988, 48, 88–96. [https://doi.org/10.1016/0010-4655\(88\)90026-4](https://doi.org/10.1016/0010-4655(88)90026-4)
16. Radjai, F.; Dubois, F. *Discrete-Element Modeling of Granular Materials*; Wiley-ISTE: London, UK, 2011. [https://doi.org/10.1016/0010-4655\(88\)90026-4](https://doi.org/10.1016/0010-4655(88)90026-4)
17. Pöschel, T. & Schwager, T. *Computational Granular Dynamics: Models and Algorithms* (Springer, Berlin, 2005). <https://doi.org/10.1007/s10035-006-0226-5>
18. Dmitriev, A.I.; Nikonov, A.Y.; Filippov, A.E.; Psakhie, S.G. Molecular dynamics study of the evolution of rotational atomic displacements in a crystal subjected to shear deformation. *Phys. Mesomech.* 2019, 22, 375–381. <https://doi.org/10.1134/s1029959918050065>
19. Österle, W.; Dmitriev, A.I.; Klotz, H. Possible impacts of third body nanostructure on friction performance during dry sliding determined by computer simulation based on the method of movable automata. *Tribol. Int.* 2012, 48, 128–135. <https://doi.org/10.1016/j.triboint.2011.11.018>
20. Rudge, R.E.D.; van de Sande, J.P.M.; Dijkstra, J.A.; Scholten, E. Uncovering friction dynamics using hydrogel particles as soft ball bearings. *Soft Matter* 2020, 16, 3821–3828. <https://doi.org/10.1039/D0SM00080A>
21. Alazemi, A. Experimental study of the lubrication mechanism of micro-spherical solid particles between flat surfaces. *Lubricants* 2021, 9, 81. <https://dx.doi.org/10.3390/lubricants9080081>
22. Paul, W.B. Molecular dynamics simulation, elementary methods. *Adv. Mater.* 1993, 5, 223–225. [https://ui.adsabs.harvard.edu/link\\_gateway/1993AdM.....5..223P/doi:10.1002/adma.19930050319](https://ui.adsabs.harvard.edu/link_gateway/1993AdM.....5..223P/doi:10.1002/adma.19930050319)

23. Fermi, E.; Pasta, J.R.; Ulam, S.M. Studies of nonlinear problems. Collect. Work. E. Fermi 1955, 2, 978–988.  
<https://doi.org/10.2172/4376203>
24. Langevin, P. On the theory of Brownian motion. C. R. Acad. Sci. Paris 1908, 146, 530–533.  
[https://ui.adsabs.harvard.edu/link\\_gateway/1997AmJPh..65.1079L/doi:10.1119/1.1872](https://ui.adsabs.harvard.edu/link_gateway/1997AmJPh..65.1079L/doi:10.1119/1.1872)
25. Landau, L.D.; Lifshitz, E.M. Mechanics: Course of Theoretical Physics, Vol. 1; Pergamon Press: Oxford, UK, 1976. [Amazon.com: Mechanics: Volume 1 \(Course of Theoretical Physics S\): 9780750628969: Landau, L.D., Lifshitz, E.M.: Bücher](#)
26. Filippov, A.E.; Popov, V.L. Numerical simulation of dynamics of block media by movable lattice and movable automata methods. Facta Univ. Ser. Mech. Eng. 2023, 21, 553–562.  
<https://doi.org/10.22190/FUME220327020F>

**Disclaimer/Publisher’s Note:** The statements, opinions and data contained in all publications are solely those of the individual author(s) and contributor(s) and not of MDPI and/or the editor(s). MDPI and/or the editor(s) disclaim responsibility for any injury to people or property resulting from any ideas, methods, instructions or products referred to in the content.